EINDHOVEN UNIVERSITY OF TECHNOLOGY
Eindhoven University of Technology

MASTER

Trajectory planning for ceramic vat photopolymerization

Wu, Z.

Award date:
2018

Link to publication

Disclaimer
This document contains a student thesis (bachelor's or master's), as authored by a student at Eindhoven University of Technology. Student theses are made available in the TU/e repository upon obtaining the required degree. The grade received is not published on the document as presented in the repository. The required complexity or quality of research of student theses may vary by program, and the required minimum study period may vary in duration.

General rights
Copyright and moral rights for the publications made accessible in the public portal are retained by the authors and/or other copyright owners and it is a condition of accessing publications that users recognise and abide by the legal requirements associated with these rights.

- Users may download and print one copy of any publication from the public portal for the purpose of private study or research.
- You may not further distribute the material or use it for any profit-making activity or commercial gain

Take down policy
If you believe that this document breaches copyright please contact us providing details, and we will remove access to the work immediately and investigate your claim.

Download date: 12. May. 2025

Department of Mechanical Engineering
Research Group - Control Systems Technology

Trajectory planning for ceramic vat photopolymerization

Graduation Project

Zhihao Wu

Supervisors:
dr.ir. A.G. (Bram) de Jager, Associate Professor, TUe
ir. T.M. (Thomas) Hafkamp, Doctoral Candidate , TUe

Report number: CST 2018.114

Eindhoven, November 7, 2018

Trajectory planning for ceramic vat photopolymerization

Zhihao Wu
Department of Mechanical Engineering, Eindhoven University of Technology, Eindhoven, The Netherlands

***Abstract*—The shaping of ceramic products had been a tricky problem in the manufacturing field until 3D printing technologies were introduced. 3D printing technology divides the process of ceramic manufacturing into two steps: stereolithography and post-heat-treatment. stereolithography is implemented by curing the photopolymerisable resin, a slurry filled with ceramic particles, so that the cured resin can play the role of binder to build the desired 3D structure, and post-heat-treatment gives the product desired mechanical properties by binder-pyrolyzing and sintering in the oven with different temperature and heating time. However, three phenomena in the process of stereolithography lower the molding precision, which can reduce the quality of the final product. These three phenomena are *light scattering*, *cross-talk* and *print-through*. Light scattering caused by the ceramic particles changes the distribution of light intensity. The exposure of the scanned pixel also affects the exposure of neighboring pixels because of the non-strict-vertical edge of the laser radiation profile, such phenomenon is termed *cross-talk*. *Print-through* describes the error of curing caused by the residual energy of the upper layer scanning on the lower layers due to the non-feasibility of complete attenuation of the exposure. These phenomena are neglected in traditional scan trajectory planning algorithms for simplicity. To improve the printing precision, this paper introduces a novel scan trajectory planning algorithm with these three phenomena considered. The scattered intensity distribution is estimated by Monte Carlo simulation combined with Mie theory. *Cross-talk* and *print-through* problem is handled by 'feature-customized optimization method' and 'transmitted exposure compensation strategy' respectively.**

***Index Terms*—Ceramic 3D printing, trajectory planning, scattering, intensity distribution prediction, Mie theory, Monte Carlo method.**

I. Introduction

ADDITIVE manufacturing (AM) was invented in the 1980s by Charles(Chuck) Hull [1]. Originally, it was only applied in the field of prototyping, so it is also known as *Rapid Prototyping*. Because of its 3D model based feature, AM provides an approach with a seamless transfer from designing to manufacturing and a handy way for idea testing, which help on reducing design cycle and cost [3]. Besides, its manufacturing mode of layer stacking provides more degrees of freedom than traditional manufacturing methods, which allows the production of complex structures such as the intertwined helices in Figure 1.

ISO/ASTM classifies AM technologies into 8 classes: fused deposition modeling (FDM), selective laser sintering/melting (SLS/SLM), laser engineered net shaping (LENS), 3D printing (3DP), direct ink writing (DIP), laminated object manufacturing (LOM), stereolithography (SLA) and digital lightprocessing (DLP) [5], [6]. Gerald et. al. have made a comparison between these methods in [7] and SLA was one of the most promising methods in terms of printing resolution, surface quality, and mechanical properties. As a subclass of SLA, vat polymerization (VP) has been widely applied in many fields for the advantages of SLA aforementioned, such as dental ceramic processing [8]. The practical value of VP is the motivation of the research introduced here.

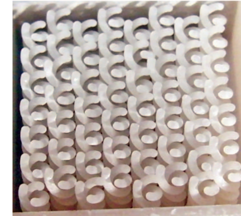

Fig. 1. An object built in refractory SiO2 ceramic by a scrolling digital mirror device. This 40-mm box has an array of 168 intertwined helices, with 56 columns of three helical rods each with $120\mu m$ diameter. Figure courtesy of Michael Middlemass, DDM Systems. Adopted from [4]

A. Introduction on previous work

In VP, the resin in the desired areas is polymerized by sufficient exposure dose from laser scanning. The cured resin holds the ceramic filler particles together to build the structure of the product. The product produced in this step is called *green part*. Subsequently, the green part is debinded and sintered with post heat treatment in oven to give the final product [9].

As shown in Figure 2, the VP process starts with the trajectory planning of cross-section scanning on the layers sliced from 3D model.

Up to now, a variety of algorithms for scan trajectory planning have been proposed and three most typical algorithms are commented in this paper, which are *WEAVE scan pattern*, *STAR-WEAVE scan pattern* and *ACES scan pattern* [3]. The first two strategies imitate the trajectory planning idea of FDM. Cured lines in VP are taken as the filaments of the same cross-section used in FDM. Such an equivalent model

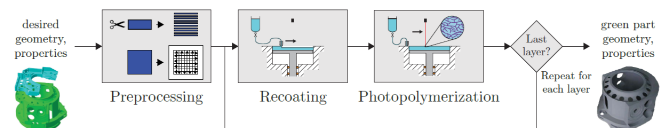

Fig. 2. VP process chain flow diagram. Adopted from [9]

neglects the exposure out of the cured region. However, the extra exposure may accumulate with the exposure from the previous or subsequent scan and leads to extra curing. Figure 3 shows the arrangement of the 'filaments'. Even though VP is a process of curing resin with proper distributed exposure, the strategies of *WEAVE* and *STAR-WEAVE* still stay on the level of material distribution arrangement essentially.

Relatively, ACES upgrades the trajectory planning idea from material distribution arrangement into exposure distribution arrangement. The aim of ACES trajectory planning is to give sufficient exposure dose in desired areas and minimize the exposure in undesired areas so that the photopolymerizable resin of the former can be fully cured and the curing happening in the latter can be minimized. Furthermore, the superposition of the exposure profiles, which are from the scan of neighboring trajectories planned by ACES, can give a more homogeneously distributed exposure as shown in Figure C.5. The homogeneity of exposure leads to the homogeneity of the cure degree, which finally determines the homogeneity of the mechanical properties on the products. Because of the aforementioned features of *ACES*, it is now more widely applied.

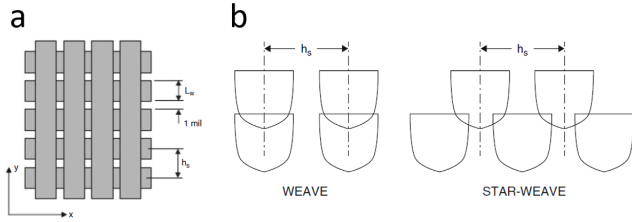

Fig. 3. a.WEAVE scan pattern; b.Cross-sectional view of WEAVE and STAR-WEAVE pattern. Adopted from [3]

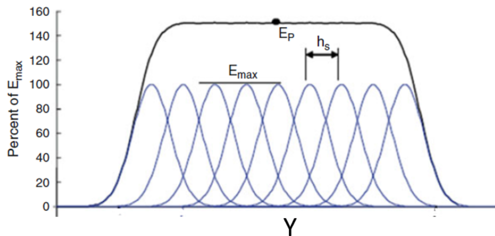

Fig. 4. Exposure profile of ACES scan pattern, Adopted from [3]

B. Research gaps and problem statement

The trajectory planning strategies based on material distribution arrangement concept shows many disadvantages, such as exposure distribution inhomogeneity and extra exposure accumulation, when it is applied in VP, which cures the resins with proper exposure distribution. So this paper gives deeper research on the strategy based on exposure distribution arrangement concept, which arranges the distribution of exposure directly.

A well-estimated intensity distribution model is the key to achieving the desired exposure distribution. Traditional trajectory planning algorithms based on exposure distribution arrangement concept, such as ACES, adopt intensity distribution model derived according to Beer-Lambert Law described by (1). $I(x, y, 0)$ is the light intensity at the point specified by coordinates x and y on the top surface of the slurry; z is the depth of the layer where the intensity is calculated; D_p is termed as *penetration depth*, which is defined as the depth at which the intensity is $1/e$ of its value on the surface [3].

$$I(x, y, z) = I(x, y, 0)e^{-z/D_p} \quad (1)$$

However, three factors are found causing intensity prediction error in ceramic 3D printing, which are *light scattering*, *cross-talk* and *transmitted exposure*. The trajectory planned with ACES based on the intensity estimation with significant errors finally results in the significant errors of the exposure distribution and mistaken curing of the *green parts*. The scattering phenomenon is caused by the particles in the resin and its occurrence disperses the energy from laser scanning, which finally results in the curing of a wider but shallower region than the curing predicted with the intensity distribution model given by Beer-Lambert law in (1). An example of curing area variation caused by scattering is shown in Figure 5. *Cross-talk* comes from the non-strict vertical edge of the exposure profile as shown in Figure 6. The exposure dose out of the scanned pixel has the same effect as the extra exposure of the planning strategies based on material distribution arrangement concept, which can accumulate to cause mistaken curing in the undesired area. And *transmitted exposure* is the residual energy from upper layer scanning as shown in Figure 7. The accumulated transmitted energy can cause additional curing on the lower layers. This phenomenon is termed *print-through* phenomenon [2].

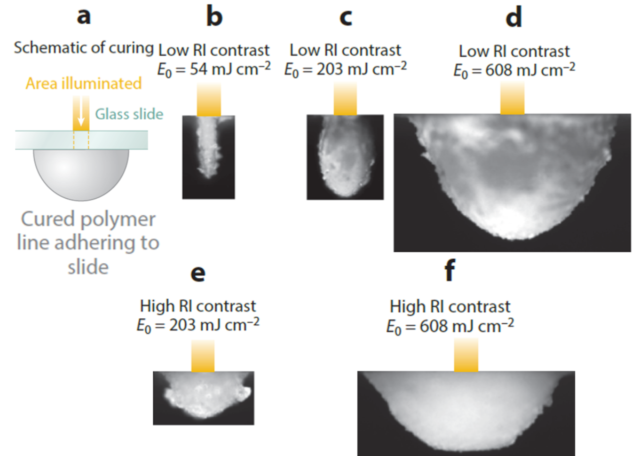

Fig. 5. Shape of the cured line in SiO_2 suspensions with varying refractive index (RI) values for monomer solution. Panel a illustrates how a square-wave beam from a slit propagated into the suspension through a glass slide cures a broadened line. The cured line shape is similar to the square wave with low RI contrast (panel b) but is increasingly broadened with higher RI contrast (panels c-f). The scale bar (500 μm) applies to panels b-f. Adapted from [4]

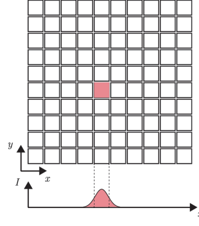

Fig. 6. Irradiation profile exceeds the boundaries of a single pixel. Adopted from [9]

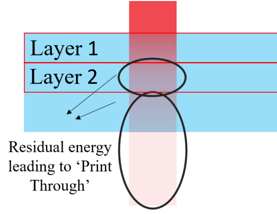

Fig. 7. Residual exposure from upper layers. Adopted from [9]

For simplicity, traditional trajectory planning algorithms neglect these three factors, which reduces the printing precision.

The novel contribution of the author's work is as follows. The author proposed a strategy based on feature disassembling and least square optimization customized for the features. Moreover, a top-down trajectory planning sequence is proposed and proved by the simulation result to be efficient for suppressing the error caused by *print-trough*. Monte Carlo method and Mie scattering theory are introduced for the estimation of the scattered intensity distribution model, whose estimation result is preliminarily proved logical by the comparison between the simulation result and experimental results given in the literature. But more experimental validations are required for proving the reliability of its estimation result.

The model adopted for the description of the polymerization is the *exposure threshold model* [3], which considers the resin in the region with exposure higher than a specific value E_c is cured. E_c is termed *critical exposure*.
The outline of this paper is as follows. The paper starts with an illustration of the intensity estimation method in Section II. Subsequently, Section III gives a detailed introduction on DFBTP method. Finally, conclusion and future work is presented in Section IV.

II. Intensity Estimation with Monte Carlo model

A. Probability density function derived with Mie theory

The importance of a well-estimated intensity distribution model has been illustrated in the last section, and the significant effect of scattering on intensity distribution prediction is also presented there. In this section, a novel method is presented to provide a more reliable intensity estimation for the trajectory planning in the next section.

The scattering phenomenon is caused by particles in the resin [4]. To estimate the distribution of intensity, Mie theory [10], [13], which describes the intensity distribution of single particle scattering, is introduced. The particles are assumed as the spheres of same radius R for simplicity. As shown in Figure 8, a linearly polarized ray, whose electric field oscillates in $\pm x$ direction, propagates in the direction of $+z$ in a homogeneous medium with a refractive index of n_m. The light is scattered by a spherical particle of refractive index n_s and radius R at the origin. The intensity of the scattered light in the direction specified by scattering angles θ and ϕ are given by (2) [20], where λ is the wavelength of the incident light and I_0 is its intensity. S_1 and S_2 are the elements on the diagonal of Jones matrix [11] whose off-diagonal elements are simplified to 0 in the case of the spherical scatterer [11], [21], [26].

$$\begin{aligned} I(\theta,\phi) &= I_0 \frac{\lambda^2}{8\pi^2 R^2}\ K(\theta,\phi) \\ K(\theta,\phi) &= |S_1(\theta)|^2 \sin^2\phi + |S_2(\theta)|^2 \cos^2\phi \end{aligned} \tag{2}$$

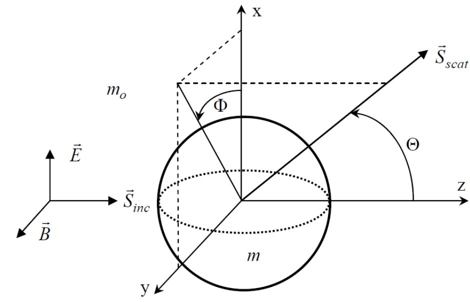

Fig. 8. Coordinate geometry for Mie scattering. Adopted from [10]

The detailed expression o

$$\begin{aligned} S_1(\Theta) &= \sum_{n=1}^{\infty} \frac{2n+1}{n(n+1)}[a_n \cdot \pi_n(\cos\theta) + b_n \tau_n(\cos\theta)] \\ S_2(\Theta) &= \sum_{n=1}^{\infty} \frac{2n+1}{n(n+1)}[b_n \cdot \pi_n(\cos\theta) + a_n \tau_n(\cos\theta)] \end{aligned} \tag{3}$$

a_n and b_n are expressed in terms of *Riccati-Bessel* function $\Psi_n(x)$ and $\xi_n(x)$ in (4) [20], where $x = \frac{2\pi R}{\lambda}$ and m is the relative refractive index given by $m = n_s/n_m$. $\Psi_n'(x)$ and $\xi_n'(x)$ are the first-order derivatives of $\Psi_n(x)$ and $\xi_n(x)$ respectively.

$$\begin{aligned} a_n(x) &= \frac{\Psi_n'(mx)\Psi_n(x) - m\Psi_n(mx)\Psi_n'(x)}{\Psi_n'(mx)\xi_n(x) - m\Psi_n(mx)\xi_n'(x)} \\ b_n(x) &= \frac{m\Psi_n'(mx)\Psi_n(x) - \Psi_n(mx)\Psi_n'(x)}{m\Psi_n'(mx)\xi_n(x) - \Psi_n(mx)\xi_n'(x)} \end{aligned} \tag{4}$$

For unpolarized incident light, $K(\theta,\phi)$ is simplified to $K(\theta) = (|S_1(\theta)|^2 + |S_2(\theta)|^2)/2$, i.e., $I(\theta,\phi)$ is only dependent on scattering angle θ and $I(\theta) \propto (|S_1(\theta)|^2 + |S_2(\theta)|^2)$ [21]. The intensity of the light in a specific direction is proportional to the number of scattered photons in this direction, so the probability density of the photons to be scattered towards the direction of scattering angle θ_0 can be calculated by (5), which

is the probability density function (PDF) of the scattering angle θ.

$$P(\theta_0) = \frac{K(\theta_0) \cdot (2\pi \sin\theta_0)}{\int_{\theta=0}^{\theta=\pi} K(\theta) \cdot (2\pi \sin\theta) \cdot (d\theta)} \quad (5)$$

B. Monte Carlo Simulation

The PDF derived in Subsection II-A gives the probability of a photon to be scattered towards the direction of scattering angle θ. However, in case of the high solid load slurry (usually higher than $50vol\%$ [15]) of VP, the photons usually experience multi-scattering before getting absorbed. So Monte Carlo method is adopted to simulate the distribution of the photon absorption points after the random scattering subscribing to the PDF given by (5).

Two processes are simulated by Monte Carlo simulation, which are *light scattering* and *light absorption*. A packet with N photons is generated and shot into the suspension vertically. Because all simulations in this paper adopt a Gaussian incident beam, the photon distribution in the dimension of radius r subjects to the PDF given by (6), where W_0 is the Gaussian radius of incident laser beam.

$$P_r(r) = e^{-2r^2/W_0^2} \quad (6)$$

Subsequently, all the photons are traced until they are all absorbed or escape from the top surface of the slurry. The coordinates of the absorption points are recorded in matrix $C_{abs} \in R^{3\times N}$.

For the simulation of scattering, two PDFs are considered, which are scattering PDF and scattering angle PDF. The scattering PDF gives the probability of a photon to travel further than a given length l before getting scattered and it can be described by (7) [14].

$$P_s(l) = e^{-l/\lambda_s} \quad (7)$$

λ_s is the mean free path of photon scattering and can be calculated by (8) [22], where r is the average radius of the particles, Φ is the solid volume fraction and Q_s is scattering coefficient. The value of Q_s can be derived from the expansion coefficients a_i and b_i of Mie theory as given by (9) [25]. Because distribution of scattering free path subjects to *Poisson distribution* [27], so there are approximately $1 - e^{-dl/\lambda_s}$ of the remained photons being scattered.

$$\lambda_s = \frac{4r}{3\Phi Q_s} \quad (8)$$

$$Q_s = \frac{2}{x^2} \sum_{j=1}^{\infty} (2j+1) Re(a_j + b_j) \quad (9)$$

The scattering angle PDF determines the scattering direction probability of the scattered photons.

The absorption follows a similar rule as the scattering. The probability of photos to travel further than the distance l before getting absorbed is given by (10) and there are approximately $1 - e^{-dl/D_p}$ of the remaining photons get absorbed after traveling a distance of dl.

$$P_a(l) = e^{-l/D_p} \quad (10)$$

In conclusion, four PDFs are considered in the simulation of Monte Carlo simulation. These PDFs are photon distribution PDF (6), scattering PDF (7), scattering angle PDF (5) and absorption PDF (10). The process of Monte Carlo simulation is shown in Figure 9.

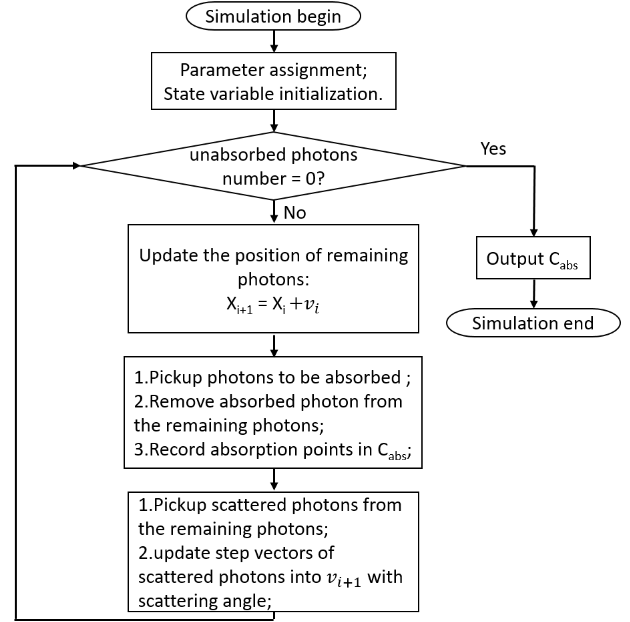

Fig. 9. Flowchart of Monte Carlo simulation

C. Simulation result

In the simulation of this project, a laser of the wavelength $\lambda = 405nm$ is adopted, the incident power P_{l0} of the laser is $10mW$ and its Gaussian radius W_0 equals to $50\mu m$, the slurry consists of the resin with refractive index $n_m = 1.45$ and $\Phi = 50vol\%$ Al_2O_3 particles with refractive index is $n_s = 1.75$. Average particle radius is $R = 2.5\mu m$. The penetration depth of the pure resin D_{p0} is $119\mu m$ The simulation gives a cloud diagram of the absorption points as presented in Figure 10.

Light intensity at a specific point is proportional to the volume density of the absorption points there. For estimating the intensity distribution with scattering phenomenon, the absorption density $\rho_s(x, y, z)$ distribution with scattering effect considered and the ratio between the light intensity and absorption density $R_i a$ are needed. The former can be calculated by dividing the number of absorption points enclosed in the sample cell by cell volume. The latter is calculated by dividing the peak intensity value of the incident light $I_i(0, 0, 0)$ by the absorption density ρ_{ns} at that point, which is simulated without scattering effect considered. Estimated intensity distribution is given by (11).

$$\begin{aligned} I_e(x, y, z) &= \rho_s(x, y, z) \; \frac{I_i(0, 0, 0)}{\rho_{ns}(0, 0, 0)} \\ I_i(0, 0, 0) &= \frac{2P_{l0}}{\pi W_0^2} \end{aligned} \quad (11)$$

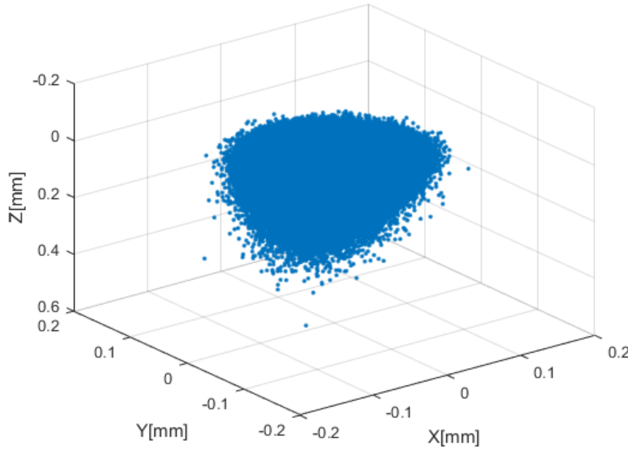

Fig. 10. Cloud diagram of absorption points

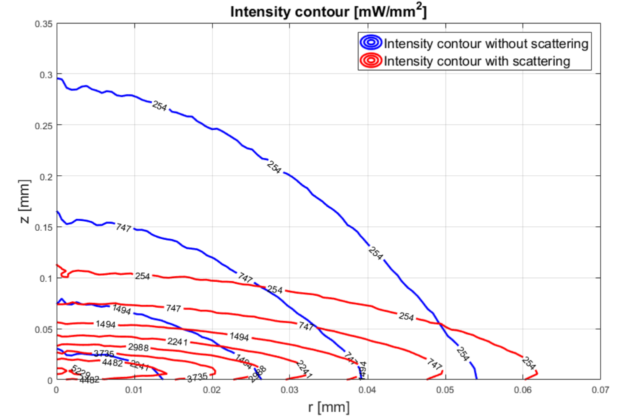

Fig. 11. Contour of the intensity distributions. The parameters for simulation is: $P_{l0} = 10[mW]$, $\lambda = 405[nm]$, $W_0 = 50[\mu m]$, $Dp_0 = 119[\mu m]$, $n_m = 1.45$, $n_s = 1.75[mW]$, $R = 2.5[mm]$

Because of the isotropy of the scattering parameters such as photon distribution and scattering angle PDF w.r.t. the z axis, the isoline of estimated intensity with scattering should also be rotationally symmetric w.r.t. the z axis. The contours of the intensity in the radial direction $r = \sqrt{x^2 + y^2}$ and the depth direction z is given in Figure 11. The blue contour is that of the intensity without scattering and the red one is the contour with scattering considered. By comparing these two contours, it can be found that the scattering shallows the cured depth and broadens the cured width with the same incident energy dose, which coincides with the experimental results reported in the literature. Besides, the cured width with broadening reaches the maximum beneath the resin surface, which gives a 'neck' structure and the 'neck' structure is relatively more obvious in the case of small exposure dose. This prediction coincides with the exposure results of different energy dose given by Halloran [5]. In Figure 5, a cured area in the shape of olive can be obviously observed with small energy dose exposure but can hardly be observed in the curing of large exposure dose. This structure has also been reported in the paper of Gentry [15].

The intensity distribution on the planes of different depth are fitted with Gaussian function $I_e(r, z) = I_e(0, z)e^{-2r^2/W_e(z)^2}$ individually. The variation of Gaussian radius $W_e(z)$ with z is shown in left subplot of Figure 12 and that of the amplitude $I_e(0, z)$ are given in right subplot of Figure 12. The right subplot of Figure 12 shows that the Gaussian radii are close to that of the case without scattering. The left subplot in Figure 12 shows the peak value does not appear on the surface $z = 0$ but slightly beneath the surface. In the region of depth larger than z_{max}, $I_e(0, z)$ still subjects to Beer-Lambert law with a smaller penetration depth D_e compared with that of the case without scattering. Besides, the peak value of $I_e(0, z)$ of the case with scattering is larger than that without scattering, which gives the reason why the cure width with scattering is larger than that without scattering even if the former also subjects to the Gaussian distribution with almost same Gaussian radius. Because the Gaussian radii of different

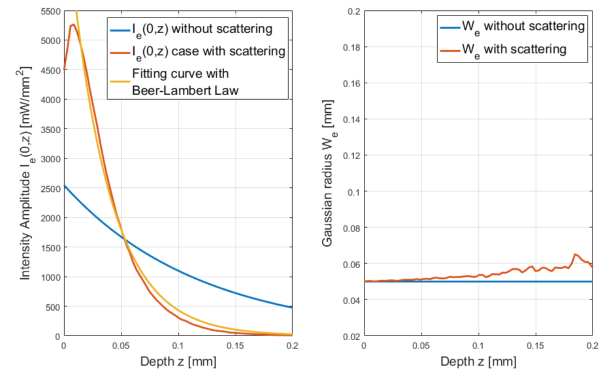

Fig. 12. Amplitudes of intensity $I_e(0, z)$ and Gaussian radii W_e on the plane of different depth z

layers has a small variation w.r.t the non-scattered radius and the amplitude curve subjects to Beer-Lambert law after z_{max}, it is reasonable to fit the scattered intensity distribution with (12) to simplify the exposure prediction in trajectory planning.

$$I_{e3D}(r, z) = I_{e3D}(0, 0)e^{-\frac{2r^2}{W_{e3D}^2}} e^{-\frac{z}{D_{e3D}}} \tag{12}$$

The contour of the fitting intensity distribution is compared in Figure 13. It can be found that the Gaussian function fits the intensity distribution model quite well in the far field. However, the intensity close to the r axis is badly approximated because of the downward offset of maximum intensity center. The intensity distribution model estimated here will be adopted for the planning of scan trajectory in the remainder of this paper.

III. Disassembled-Feature-Based Trajectory Planning

The error caused by the first factor *light scattering* is reduced by adopting the more accurately estimated intensity distribution model given by the simulation in Section II for scan pattern planning. For further improvement on the printing precision, Disassembled-feature-based trajectory

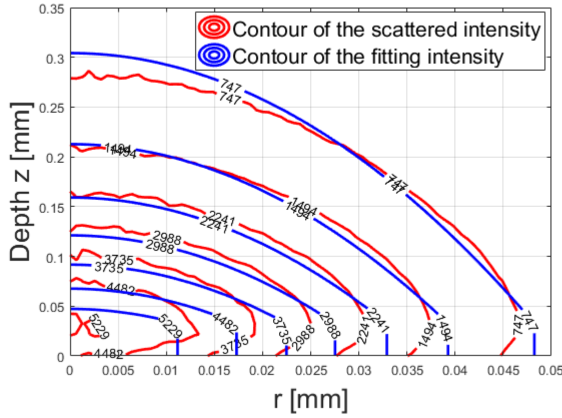

Fig. 13. Contour of the scattered intensity and the fitting intensity

planning (DFBTP) algorithm is introduced in this section for minimizing the effect of the other two factors.

The idea of DFBTP algorithm is inspired by that of *Optical proximity correction (OPC)*, and the latter has been widely applied in today's integrated circuit (IC) manufacturing [12]. OPC provides a strategy to compensate for the error caused by the non-ideal optical and process effects by modifying the Layout patterns on the masks. An intuitive example is presented in Figure 14. The comparison between the simulated images given by the exposure of the layout patterns with and without OPC proves the improvement given by OPC on the fidelity of pattern transfer to the wafer.

OPC is classified into *model-based* OPC and *rule-based* OPC. The former one can provide the features with geometry-customized modification plan by simulation, which can handle the planning of complex geometries. However, it is quite time-consuming. The other one can give a faster planning by comparing the geometric features of the target images with the features in a look-up table and assembling the solutions for individual features. The solutions in the look-up table are pre-computed or acquired by experiments. The disadvantage of this method is the limited number of solution number in the look-up table. On the one hand, the complexity of the products to be printed by VP requires more flexibility of the planning algorithm, but on the other hand, too much time cost is not acceptable. So this paper proposes DFBTP algorithm, which combines the advantage of these two OPC methods.

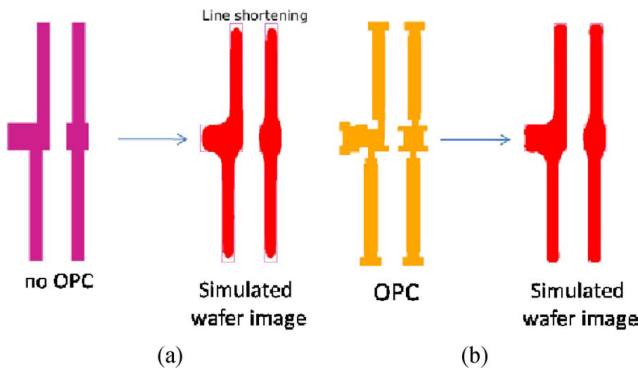

Fig. 14. (a) Layout pattern without OPC and simulated image on wafer. (b) Layout pattern with OPC and simulated image on wafer Adopted from [12]

The images to be printed are disassembled into blocks and each block contains only one feature, such as a corner, a linear edge or the middle area of the image. Subsequently, we mesh the blocks to discretize the continuous scanning process on the real devices into a process of illuminating grid points with different exposure times. The exposure times of the grid points are the design variables in the optimization of the scan patterns. To reduce the time cost of the planning process, the optimization problem is customized according to the geometric complexity of the feature. The features with higher complexity are given more degrees of freedom for designing. Moreover, the sequence of the layer trajectory planning of the traditional algorithms such as ACES is in a sequence of top-to-bottom normally. However, an inverse sequence is adopted in DFBTP algorithm to get the information of the transmitted exposure from upper layer scanning so that it can be compensated in the planning of lower layers for reducing *print-through*.

The process of trajectory planning is shown in Figure 15. The rule of feature disassembly is given in Subsection III-A. Subsection III-B describes the planning of the scan patterns for different features. The result given by scan pattern planning are the coordinates of the points to be scanned and the local exposure times there. For controlling the device to illuminate the points described by in by scan patterns, an array which gives the coordinates of the pointsto be visited sequentially by laser spot on trajectory is needed and it is presented in Subsection III-C. In the case of 3D printing, transmitted exposure from upper layers needs to be considered in trajectory planning, and a transmitted exposure compensation strategy is proposed in Subsection III-D. The effectiveness of the DFBTP method is evaluated in Subsection III-E

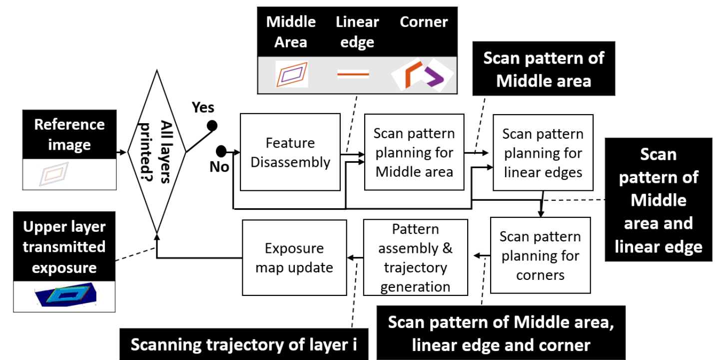

Fig. 15. Process of trajectory planning with DFBTP

A. Feature disassembly

For implementing the geometry-customized optimization, a good partitioning of the feature blocks is important. In this paper, we discuss the scan pattern optimization of three features: *the middle area*, *linear edge* and *corner*.

For reducing the time cost of scan pattern optimization, the main area of the image is planned to be scanned with ACES scan pattern for the good exposure homogeneity it can achieve.

The area scanned with ACES pattern is defined as *middle area* and the boundary of the middle area is defined as the boundary where the exposure from middle area scanning reduced to $5\%E_p$ as shown in Figure 16. ACES can achieve homogeneous exposure distribution in the middle part, but there is always such an area affected by the *side effect*. *Linear edge* is the area between the straight line boundary and affected by the *edge effect* in the direction perpendicular with the straight line boundary. The scan pattern of the linear edge is designed to compensate the insufficient exposure w.r.t. the reference value E_{tar} in this area. Because the exposures of the grid points in the same row aligned with the straight line boundary are same but vary in the vertical direction, the optimization of the linear edge is posed as as a one-dimensional problem, which only has the grid points exposure times of one column as design variables.

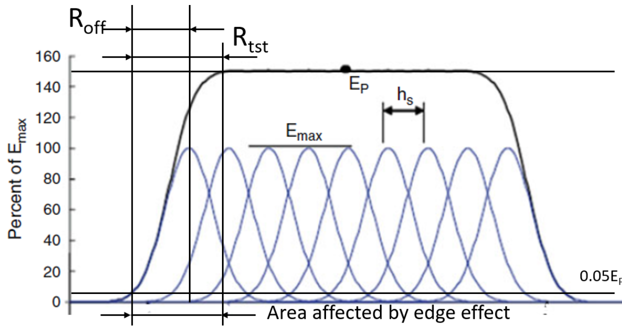

Fig. 16. Exposure profile achieved by ACES scanning. Adopted from [3]

Corner area is defined as the area affected by the side effect in more than one directions. The geometric complexity of corner area is higher than that of the linear edge and middle area, the exposure times of all grid points are manipulated as design variables. So the DOF of corner area design the highest among the aforementioned three features. Linear edge takes the second place and that of the middle area design is the least. The sequence of scan pattern plan starts with the plan of the feature with the least DOF of design, which is the middle area here, Because if the lower DOF feature is planned after the planning of other features, it does not has enough design variables to be manipulated to fit the profile of the exposure map to be compensated by its scan pattern plan.

Now that the planning starts with the middle area, the partition of the middle area is introduced first. For minimizing the time cost of the trajectory planning simulation, planning method with low DOF is applied as much as possible. So we try to maximize the size of the middle area so that the exposure to be compensated by other two time-consuming methods can be minimized. The partition of the middle area is given in Figure 17 as the purple outlines, the boundary of the middle area is acquired by offsetting the boundaries of the reference image towards the inner side by R_{off}. Thus the edge of $5\%Ep$ overlaps with the boundaries of the reference image and the scan of linear edge and corner only needs to compensate the area affected by the edge effect. The value of R_{off} is given by (13), which is dependent on the value of the Gaussian radius W_{e3D} of the intensity distribution and hatching space factor $r_h = h_s/W_{e3D}$. $\mathbf{a} = [a_0, a_1, a_2]^T$ is the coefficients of the quadratic fitting polynomial. For a detailed illustration on the derivation of R_{off} please refer to Appendix A. R_{tst} is named *transition distance*, which is defined as the distance from point of $5\%E_p$ to the first point where the gradient of exposure is 1% of the maximum as shown in Figure 16and R_{tst} describes the width of the region where the value of middle area exposure decreases from the homogeneous value E_p to a negligible value $5\%E_p$.

$$R_{off} = (a_2 r_h^2 + a_1 r_h + a_0) W_{e3D} \tag{13}$$

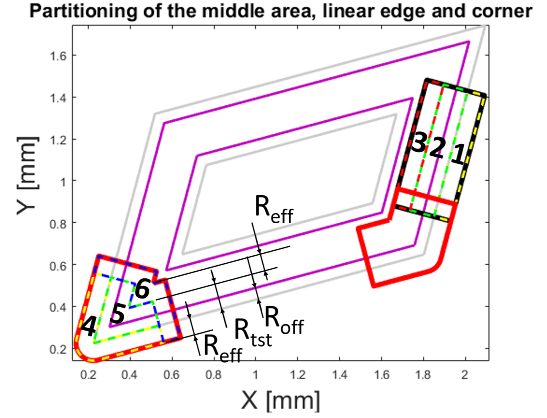

Fig. 17. Sketch of the feature-based partition. Gray outline: the boundary of the reference image. Purple outline: the boundary of the middle trajectory planning area. Black solid curve: the boundary of the linear edge area. Red solid curve: the boundary of the corner area

With the exposure map from the middle area scanning known by adding the exposure contribution of the scanning of the middle area points together, the scan pattern of linear edges are designed to compensate the insufficient exposure w.r.t. the target exposure value E_{tar}. The block of the linear edge consists of three subblocks, which are numbered with 1, 2 and 3 in Figure 17. Subblock 2 is the area affected by the *side effect* as shown in Figure 16. Subblock 1 is an extension of the linear edge designing area towards the area out of the desired area given by the reference image. Extension distance R_{eff} is termed *effective radius* and it is the distance at which the exposure of a dot exposure attenuates to a negligible percentage (lower than 1%) of its center exposure. So subblock 1 encloses all points whose exposure can affect subblock 2 and the exposure times of these points can be manipulated as design variables in the optimization of linear edge scan pattern planning to improve the exposure distribution of subblock 2. Subblock 3 is another extension of subblock 2 but towards the inner side. This subblock encloses all points whose exposure has achieved the target value in the middle area. Because they are within the effective radius of the scanned points in subblock 2, so the exposure in subblock 2 may add additional exposure on the points in subblock 3, which may increase the printing error from printing through and is not desired. So the exposure of the points in subblock 3 are also included in the optimization of linear edge scan pattern to limit the additional exposure in this region.

The partitioning of the corner feature, which is given as the red solid line in Figure 17, follows the same idea of the linear edge partitioning. The overlapping area between the corner block and that of the linear edge is the area affected by the *side effect* of the linear edge scanning. Subblock 5 and subblock 6 are the external and internal extension of subblock 5. Their functions are same as that subblock 1 and subblock 3 have in the linear edge partitioning.

B. Local scan pattern planning

In order to minimize the time cost of scan pattern planning, the optimization problems of different features are customized according to its geometric complexity. The introduction given here includes the strategies for *the middle area*, *linear edge* and *corner*, whose partitions have just been given.

1) Scan pattern planning for the middle area: The scan pattern adopted by the middle area is ACES which has only three variables: scanning direction $\vec{v}$, scanning velocity V_s and hatch space h_s. The value of the maximum allowed hatching space is determined by the requirement on exposure homogeneity. In this paper, the homogeneity of the exposure is described with relative standard deviation given by $S_{rlt} = S_{exp}/E_{tar}$, where S_{exp} is the allowed standard deviation of the exposure. The value of the target exposure value E_{tar} adopted is given by (14) to ensure the exposures of the points at different depths within the layer being scanned larger than the critical exposure E_c so that the resin at different depth of a same layer can be cured. And $h = l_t - z_{max}$, l_t is the layer thickness.

$$E_{tar} = E_c/e^{-h/D_{e3D}} \tag{14}$$

The value of the hatching space is given in (15). $\lceil \bullet \rceil$ here is ceiling function, and $\mathbf{c} = [c_1, c_2, c_3, c_4]^T$ is the coefficient array of the fitting function, which is detailed in Appendix B.

$$h = H/\left\lceil H/\left(\left(\ln\left(\frac{\frac{1}{W_0^2}S_{rlt} - c_1}{c_2}\right) - c_4\right)\frac{W_0}{c_3}\right)\right\rceil \tag{15}$$

The scanning direction is chosen to be aligned with the longest linear edge to make the exposure distribution of the linear boundaries as homogeneous as possible. Because the case with curved boundary is beyond the scope of this paper, scanning direction determination without linear edge is not discussed here. The scanning velocity is given by (16). The detailed derivation of (16) is given in Appendix C.

$$V_s = \frac{P_l}{h_s E_{tar}} \tag{16}$$

The simulation result of the exposure from middle area scanning with ACES is given in Figure 18.

2) Scan pattern planning for linear edge: With the scan pattern of the middle area known, the insufficient exposure E_c to be compensated by linear edge scan pattern in the block of the linear edge can be calculated by subtracting the exposure of the middle area scanning from the target exposure map E_{tm}. The target exposure values of the points in the undesired area are 0 and that in the desired area is E_{tar} given

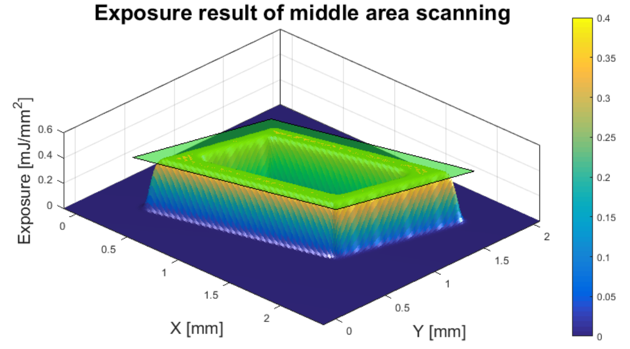

Fig. 18. Exposure map with the scanning of the Middle area

by (14). The negative elements in E_c are reset as 0 because it is impossible to apply negative exposure by scanning. The 2D map of the exposure to be compensated can be simplified into one dimensional in the direction perpendicular with the linear edge because of the homogeneity in the direction aligned with the linear edge as shown in Figure 19. As mentioned in

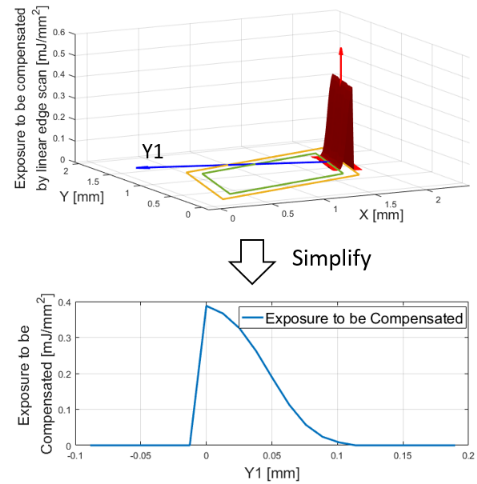

Fig. 19. The degradation of Exposure map to be compensated in linear edge block from 2D to 1D

Subsection III-A, the exposure times T_1 and T_2 of the points in the subblock 1 and 2 respectively are taken as the design variables to be manipulated in linear scan pattern optimization. And the target of the optimization is to minimize the exposure error in subblock 2 and 3, so the optimization problem is formulated as (17) shows. E_{ic} is the exposure of the points in subblock i and it is given by the scanning of the points in subblock 1 and 2. $[T_1, T_2]^T$ is the exposure time array containing the exposure times of the point in subblock 1 and 2 and K_{ij} is exposure contribution matrix given by (18) for the calculation of the exposure contribution of T_j on E_i. $I_{e3D}(r, z)$ is the intensity distribution model given by (12). X_i and Y_i are the arrays containing the x and y coordinates of the points whose exposures are calculated in subblock *i*. n_j is the number of the scanned points in subblock *j*. x_k and y_k are the x and y coordinates of the scanned points in subblock

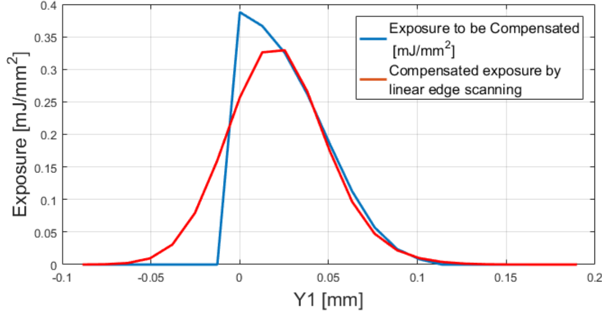

Fig. 20. Exposure compensation with linear edge scanning

j.

$$\min_{T_l>0}: \quad f\left(\begin{bmatrix}T_1\\T_2\end{bmatrix}\right) = \left\|\begin{bmatrix}K_{11} & K_{12}\\K_{21} & K_{22}\\K_{31} & K_{32}\end{bmatrix}\begin{bmatrix}T_1\\T_2\end{bmatrix} - \begin{bmatrix}E_{1c}\\E_{2c}\\E_{3c}\end{bmatrix}\right\|$$
$$s.t.: \quad \begin{bmatrix}K_{11} & K_{12}\\K_{21} & K_{22}\\K_{31} & K_{32}\end{bmatrix}\begin{bmatrix}T_1\\T_2\end{bmatrix} - \begin{bmatrix}E_{1c}+a_1E_{tar}\\E_{2c}+a_2E_{tar}\\E_{3c}+a_3E_{tar}\end{bmatrix} \leq 0 \tag{17}$$

$$K_{ij} = \sum_{k=1}^{k=n_j} I_{e3D}(\sqrt{(X_i - x_k)^2 + (Y_i - y_k)^2}, 0) \tag{18}$$

The value of the exposure to be compensated of a point equals the target exposure there minus the exposure given by the scanning of existing trajectories and the target exposure in subblock 1 and 3 are respectively 0 and E_{tar}, which are close to the exposure given by the scanning of the trajectories planned earlier. So the exposures to be compensated in subblock 1 and 3 are close to 0. And the illuminating in corner blocks will always add some exposure in this two subblocks due to cross-talk. The optimum exposure time array given by optimization would be all zero if without the upper bound lifting and all zero solution is not the solution desired. To avoid all-zero solution, the inequality constraints make the upper bounds slightly larger than the reference compensating exposure by adding a positive item a_iE_{tar}. The exposure added by linear edge scan is given in Figure 20. Insufficient exposure in the desired area are compensated with the sacrifice of overexposure in the undesired area.

3) Scan pattern planning for corner:
The optimization of corner scanning pattern is analogous to the process of linear edge scan pattern optimization, which is formulated by (19).

$$\min_{T_l>0}: \quad f\left(\begin{bmatrix}T_1\\T_2\end{bmatrix}\right) = \left\|\begin{bmatrix}K_{44} & K_{45}\\K_{54} & K_{55}\\K_{64} & K_{65}\end{bmatrix}\begin{bmatrix}T_5\\T_6\end{bmatrix} - \begin{bmatrix}E_{4c}\\E_{5c}\\E_{6c}\end{bmatrix}\right\|$$
$$s.t.: \quad \begin{bmatrix}K_{44} & K_{45}\\K_{54} & K_{55}\\K_{64} & K_{65}\end{bmatrix}\begin{bmatrix}T_1\\T_2\end{bmatrix} - \begin{bmatrix}E_{4c}+a_4E_{tar}\\E_{5c}+a_5E_{tar}\\E_{6c}+a_6E_{tar}\end{bmatrix} \leq 0 \tag{19}$$

The map of the exposure with all scan patterns is shown in Figure 21. The green semitransparent plane is the plane of reference exposure E_{tar} given by (14) and the yellow peaks over it denotes the points with exposure higher than

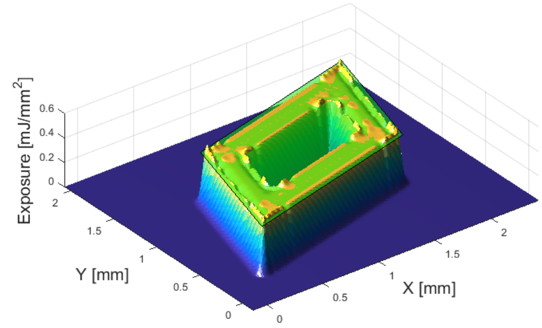

Fig. 21. Exposure map with the scanning of the middle area, linear edge and corner

the reference value. The exposure map given by pure ACES scan pattern is given in Figure 22. By comparing Figure 21 and 22, it can be found the homogeneity of exposure given by ACES is better than that given by disassembled-feature-based optimization (DFBO). However, the global error

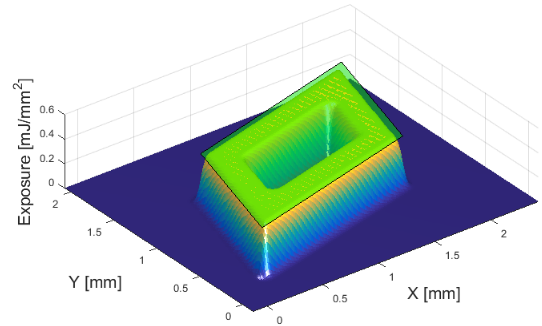

Fig. 22. The exposure map acquired by the scanning of pure ACES algorithm

can be lower by the latter algorithm according to Figure 23, where the absolute value of the exposure error ratio $R_{ero,i} = E_{ero,i}/E_{tar}$ at all points are sorted in ascending order and visualized. It can be found exposure error ratios of DFBO is lower than that of ACES even though the peak value of the former is larger. And the square summation of the exposure errors of DFBO is $39[mJ^2/mm^4]$, smaller than that of ACES method $60[mJ^2/mm^4]$.

According to the comparison above, it can be concluded that DFBO can reduce the error of exposure distribution. However, exposure homogeneity will be sacrificed because of upper-bound-lifting in (17) and (19), which causes the exposure of some points larger than the target value E_{tar}.

C. Global scanning trajectory generation

DFBO method introduced in Subsection III-B gives a coordinate set **C** of the points to be scanned in each block as well as the corresponding exposure time array **T**. To control the motion of the laser beam, a trajectory which visits all points in **C** with minimum time cost is required to control the motion

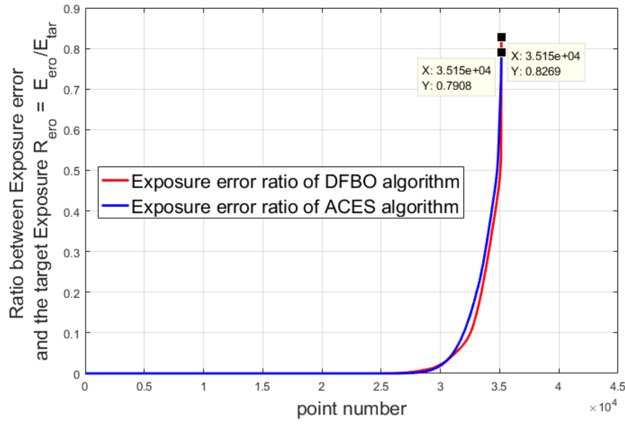

Fig. 23. Comparison between the exposure error ratios given by ACES and DFBO

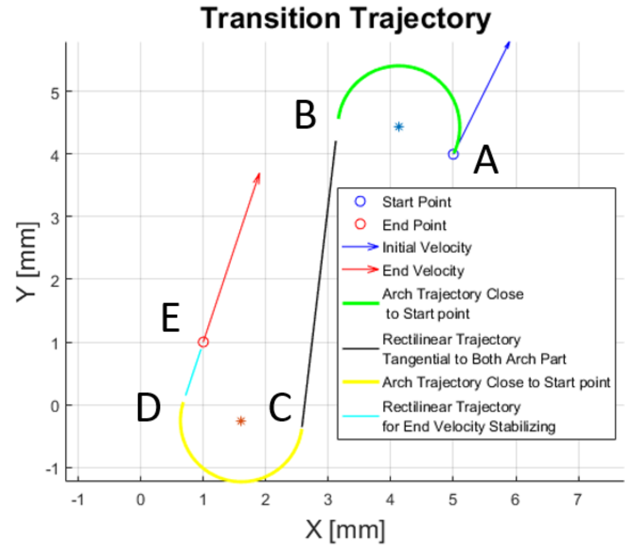

Fig. 24. The sketch of the transition trajectory design between the start point A and and point E

of the laser actuator. The trajectory should be given in the form of an array of the coordinates to be sequentially visited along the trajectory.

The scanning of the internal trajectory within a block is performed in the form of progressive scanning. To connect the trajectory of the neighboring rows, the internal transition trajectories are needed. For a smooth transition between the local trajectories of the blocks, transition trajectories are also needed. In this section, we start from the introduction of transition trajectory design. Subsequently, the further investigation on reducing time cost of scanning with the scan sequence arrangement of the local trajectories is illustrated.

1) Transition trajectory design:

To achieve a smooth transition, the trajectories designed should be tangent to the velocity at start point A and end point E as shown in Figure 24. So two arches which are tangent to the start and end velocity at A and E respective are constructed. Because of the limitation of the device on the maximum velocity v_{max} and the maximum acceleration a_{max}, the curvature of the trajectory must be larger than the maximum allowed value $\rho_{max} = \frac{a_{max}}{v_{max}^2}$. The default radius of the arc here adopts three times of the minimum allowed radius $R_{arc} = 3/\rho_{max}$. The velocities of scanning are constant in the start arch and the end arch and equal the initial velocity and end velocity respectively. $\overline{BC}$ is a line segment which is tangent to both arches and the process of acceleration from the initial velocity to the end velocity is completed in this section. However, given the coordinates of the start and end point along with the velocities at these two points, each point can find two circles of the specified radius as Figure 25 shows. So the tangential line $\overline{BC}$ has four options in this way. To find the transition trajectory with the minimum time cost, the time costs of four potential transition trajectories are calculated and the one with the minimum time cost is picked. The last section of the trajectory is a line segment for stabilizing the velocity before the scanning of the next line.

And Figure 26 shows an example of transition trajectory design which connecting the endpoint and the start point of two neighboring trajectories sequentially. And the transition trajectory connects two trajectories smoothly with continuous curvatures along it.

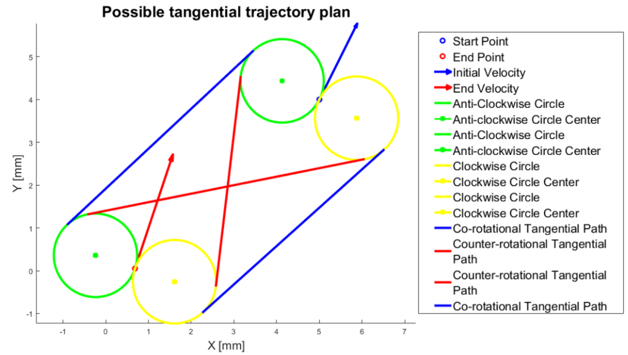

Fig. 25. Possible choices of transition trajectory

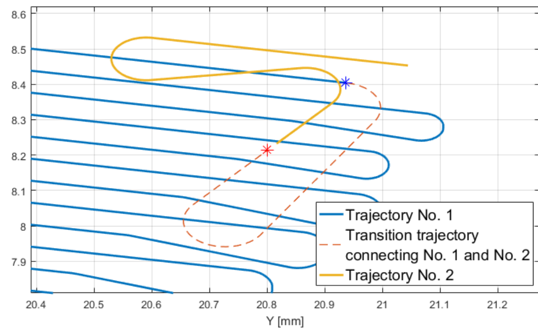

Fig. 26. A transition trajectory smoothly connecting two neighboring trajectories

2) Scanning sequence optimization of the local trajectories:

With the transition trajectory between two points planned, the time cost for transition is known. In the case of more

than one local trajectories, the sequence of local trajectories to be scanned has a significant effect on the total time cost of transition, which can be described as a general problem: *Traveling Salesman Problem(TSP)*: Given a set of points and the time cost for traveling between every pair of points, the problem is to find the route that visits every point exactly once and returns to the starting point with the minimum time cost.

For the TSP problem, three algorithms are considered, which are exhaustion method, dynamic programming and ant colony method [19]. The first method sloves the problem by listing the time cost of all possible sequence and picking up the option with minimum timecost. However, the number of possible routes explodes factorially and is not suitable for the case with large number of points to be arranged. The second reduces the number of routes to be searched to $n^2 2^n$, which is still too large and not recommended for the case with more than 13 points[16], [17], [18]. The last one is adopted in this project, which is a bionic algorithm imitating the performance of the ant colonies in food seeking.

Starting at an arbitrary point among the set, ants choose the next point according to the concentration of the pheromone left by the ants who passed these routes before. Besides, the visibility of the candidate points from current point also affect the choice of the ants. Apart from these two terms, the choices of the ants is also influenced by probabilistic nature. The influence of these factors are formulated in (20). τ_{ij} is the pheromone concentration on the route between point i and point j and point i is the current location of the ants; $\eta_{ij} = 1/d_{ij}$ denotes the visibility of point j from i, and d_{ij} is the length of route between i and j. α and β are effectiveness factors which can improve the effectiveness of the corresponding items on the the probabilities of the choices. $allowed_k$ is the set of the subscripts of the candidate points among which the choices are made. In the case of TSP, candidate points excludes the points that has been visited. Once an ant walks over a route, it leaves pheromone of concentration $\triangle\tau_{ij} = Q/d_{ij}$. The concentration of the pheromone there is updated to $\tau_{ij}(t+1) = \rho\tau_{ij}(t+1) + \triangle\tau_{ij} \times n$, where ρ is the attenuating rate of pheromone and n is the number of ants choosing route ij in the last round.

$$P_{ij}^k = \begin{cases} \frac{[\tau_{ij}]^\alpha \cdot [\eta_{ij}]^\beta}{\sum_{S \in allowed_k} [\tau_{ij}]^\alpha \cdot [\eta_{ij}]^\beta} & j \in allowed_k \\ 0 & otherwise \end{cases} \tag{20}$$

The pheromone on short route attenuates less and pheromone concentration increment given by each ant choosing the route is larger. Increasing pheromone concentration increases the probability for ants to choose this route in the next iteration; the more times it is chosen, the higher the concentration will be. It builds up a positive feedback loop that finally converges to the shortest route [19].

Optimization provided by ACO is given in Figure 27. Transition time cost is reduced by 54.41% w.r.t. initial transition time cost and 3.65% w.r.t. the time cost for the scanning of one layer. However, computation takes 7 seconds for optimization but only saves 0.0034 second. Besides, whole layer scanning time cost increases quadratically but that for transition increases linearly with the size of reference image increasing. i.e. optimization for scanning sequence optimization is less 'worthwhile' for the printing of larger images. In conclusion, printing sequence optimization is less worthwhile to be executed for small batch manufacturing.

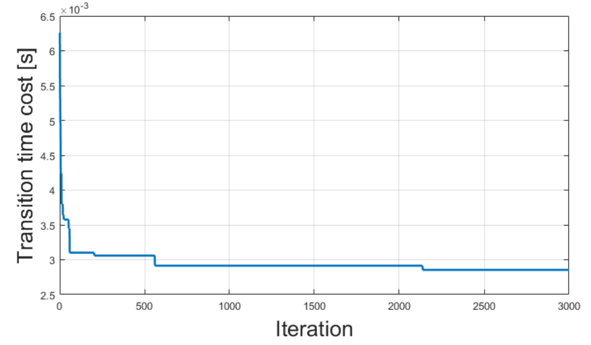

Fig. 27. Total time cost in seconds for transition between the local trajectories

D. Generalization from 2D to 3D

Transmitted exposure from the upper layer scanning needs to be considered in the scan trajectory planning for 3D model to avoid or lower the effect of *printing-through*. In order to get the information of the transmitted exposure on the lower layers, the sequence of trajectory planning is revered and starts from the top layer to bottom layer. With the scan pattern of the upper layer known, the exposure maps of the upper layer can be calculated and its effect on the lower layers can be calculated by (21), where $E_{t,i}$ is the map of transmitted exposure on layer i and $E_{map,j}$ is the exposure map given by the scanning on layer j, n is the total number of the layers.

$$E_{t,i} = \sum_{j=i+1}^{j=n} E_{map,j} e^{-\frac{l_t(j-i)}{D_{e3D}}} \tag{21}$$

So the map of the exposure to be compensated on layer i $E_{c,i}$ by the scanning on the same layer is given by (22), where $E_{tar,i}$ is the target exposure map of layer i.

$$E_{c,i} = E_{tar,i} - E_{t,i} \tag{22}$$

Figure 28 shows a map of the exposure to be compensated on layer $n-1$ by the scanning on this layer. This map is acquired by subtracting the transmitted exposure map from layer n from the target exposure map of layer $n-1$. The transmitted exposure compensation method performs well for the alleviation of the print-through problem in the printing of tapered structure. Because lower layers cross-sections of tapered structures are always larger than the projection of the upper layer cross-sections on it. So $E_{tar,i} - E_{t,i}$ can always give positive exposures to be compensated by lower layer scanning. However, for the printing of bottom-narrow structure, the cross-section of the lower layer is smaller than that of the upper layers, i.e. transmitted exposure from upper

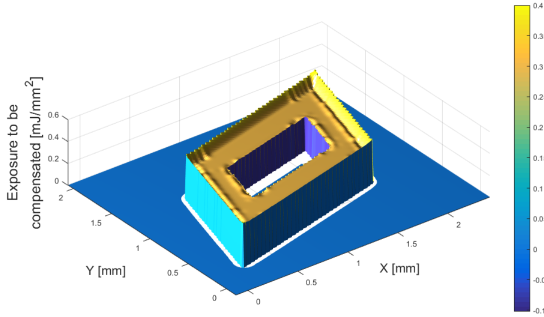

Fig. 28. Map of the exposure to be compensated on layer $n-1$ after transmitted exposure being subtracted from the target exposure map

layers can cover the undesired area on lower layers, where the target exposure is 0. So a negative compensating exposure will be given by (22). However, laser scanning can only implement positive exposure.

In conclusion, transmitted exposure compensation is a good method for alleviating the over-curing caused by transmitted exposure and theoretically can eliminate *print-through* error in the printing of the tapered structure. But for bottom narrow structure, the transmitted exposure in the undesired area of lower layers can still result in some extra curating, but it can be alleviated with proper chosen target exposure E_{tar}. For example, in Subsection III-B, target exposure is chosen as $E_{tar} = E_c/e^{-l_t/D_{e3D}}$. So the exposure has attenuated to E_c at the bottom surface of the scanned layer, the transmitted exposure in the deeper area than the bottom surface is smaller than E_c. Even though for bottom narrow structure the transmitted exposure in the undesired area cannot be compensated, its dose is not large enough to lead to severe extra curing in the depth direction.

E. Evaluation of DFBTP method

The effectiveness of DFBTP algorithm on the improvement of printing precision can be verified by the comparison of the printing result with ACES and DFBTP in Figure 29 and Figure 30. Figure 29 gives the side view of the printing results. It can be found that the over-cured area in $-z$ direction of the printing result with DFBTP is obviously shallower than that with ACES, which shows the effectiveness of the transmitted exposure compensation strategy in DFBTP. And the fidelity of the corner and linear edge are also improved according to the comparison between the contours in Figure 30 . The contour given by DFBTP scanning is apparently more close to the reference contour and the error found in corner area are also reduced. The improvement on corner area printing precision is more visible for in the corner area of larger angle, such as the bottom-left corner of the inner contour in Figure 30. In conclusion, the effectiveness of *transmitted exposure compensation* strategy have a significant effect on the reduction of the error due to *print-through*. And the strategy of reducing the error caused by *cross-talk* with feature-customized optimization also meets the goal.

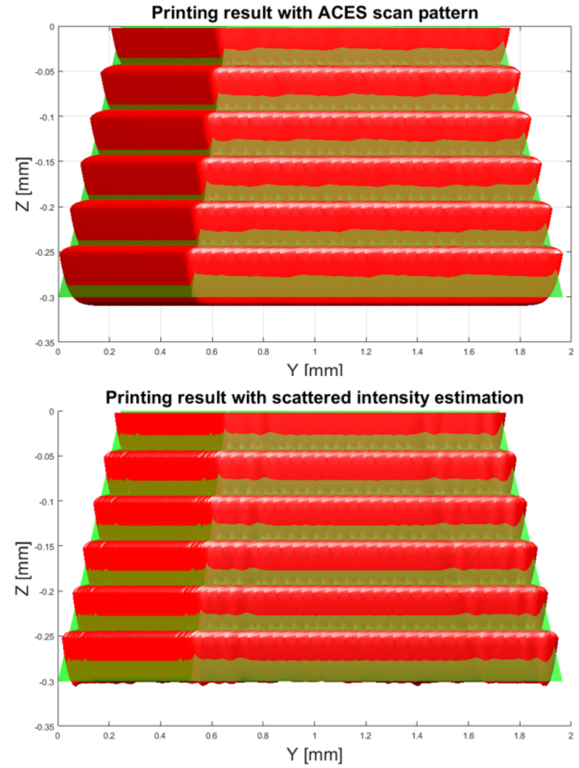

Fig. 29. Side Views of the printing results with ACES and DFBTP. The red surface is the isosurface of exposure value E_c. Green polyhedron is the reference 3D model

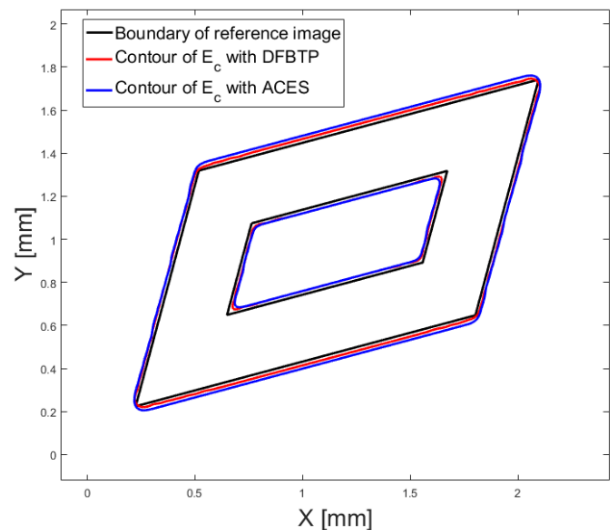

Fig. 30. Contour of the first layer exposure of the printing results with ACES and DFBTP. The exposure on contour is E_c

Figure 31 gives the comparison between the printing results with and without the scattered intensity distribution model estimated in Section II. It can be found that the trajectory designed without intensity estimation has severe shallow curing problem, which can result in the bad inter-layer adhesion and the separation of the images printed on neighboring layers. The necessity of the scattered intensity distribution model estimation is explicitly proved here.

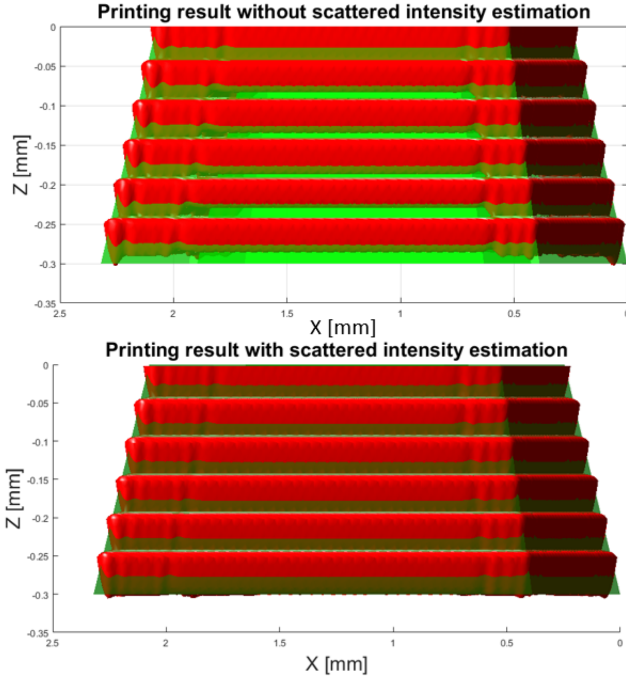

Fig. 31. Comparison between the side views of the printing results with and without scattered intensity distribution model estimation. Green polyhedrons in the image is the reference 3D model whose height is 3 [mm]. The red surface is the isosurface of exposure value E_c

IV. Conclusion and outlook

The goal of this paper was to acquire a strategy for the scan trajectory planning of ceramic vat photopolymerization. To achieve this object, intensity distribution model with particle scattering, cross-talk correction with disassembled-feature-based trajectory planning and print-through correction with transmitted exposure compensation are studied.

Monte Carlo method combined with Mie scattering theory was adopted for the estimation of intensity distribution model and the result can be qualitatively considered as logical according to the experimental results provided in the literature. However, more experimental result are needed to make further investigation on its reliability. The attempt to lower cross-talk error also meets the goal according to the comparison of the error suppression performance w.r.t. ACES scan pattern. As for the correction of print-through error with transmitted exposure compensation, the error suppression performance in the direction perpendicular to the resin surface is satisfactory and the attempt in this respect is successful. For the further studies on the improvement of vat photopolymerization print quality, error compensation with the optimization method requires a more reasonable feature partitioning strategy to handle the scan pattern planning of more complicated features such as curve edge. The significance of a reliable intensity distribution model has been proved in this paper. To acquire a more precise estimation, more details, such as the reduction of photoinitiator and dyes in the process of exposure, should be included in the future. Print-through correction by transmitted exposure compensation with the information of upper layer exposure distribution requires more research on how to implement in the real setup with the problem that the insufficient exposure of the lower layer may not be strong enough to allow the operation such as re-coating. Verifying its feasibility on real devices requires more experiments.

transition trajectory

Appendix A
Derivation of R_{off} in numerical method

It is mentioned in III-A that the optimization of the scan patterns of corner and linear edge is more complex and time consuming w.r.t. that of the middle area. A well chosen offset distance R_{off} for the middle area partitioning can minimize the size of the area left to be compensated by the scan pattern optimization of linear edge and corner area, which reduces the time cost for scan pattern optimization. The scan pattern adopted by the middle area scanning is ACES for the exposure homogeneity.

The definition of the outer boundary of the exposure map is the location where exposure value is $0.05E_p$ and E_p is the exposure value in the middle area ss shown in Figure A.1. When the offset distance R_{off} equals the distance between the point where the exposure equals $0.05E_p$ and the center of the first scanning line, the outer boundary of the exposure map of the middle area scanning just overlaps with the boundary of the reference image and for the area left for corner and linear edge optimization, the minimum width is achieve.

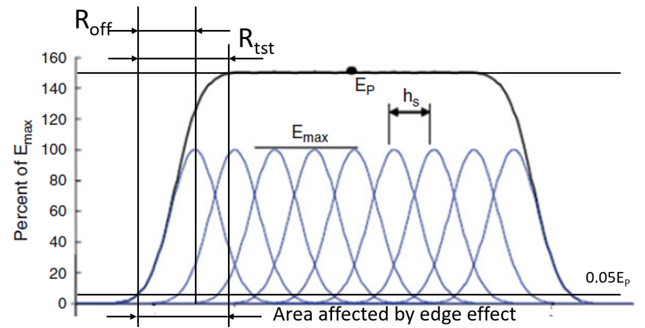

Fig. A.1. exposure of the ACES scan pattern. Adopted from [3]

In the derivation of R_{off} with numerical method, a function of hatching space ratio $r_h = \frac{h_s}{W_0}$ is given to calculate R_{off}. Hatching ratio r_h is defined because the R_{off}/W_0 is a polynomial of r_h with coefficients independent with W_0 and the function independent with the Gaussian radius can be more widely applied only if the intensity distribution is Gaussian.

The numerical solving process starts from calculating the

exposure profile with a given normalized Gaussian light distribution $I(a) = e^{-\frac{y^2}{W_0^2}}$ and hatching space ratio r_h. With exposure profile computed and the first coordinate of the center of Gaussian profile c_1 know, the coordinate of the first point of exposure value $0.05E_p$ can be found and denoted by variable $b_{0.05}$. The distance between $b_{0.05}$ and c_1 denoted by variable $|bc|$ is actually theR_{off} we are looking for. Divide $|bc|$ by W_0 to give the dimensionless transition distance R'_{off} so that the fitting function derived can be applied to the cases with different Gaussian radius for R_{off} calculation. Calculate the values of R'_{off} with different r_h in the interval $[0, 1]$ and their relationship is given in Fig. A.2. Quadratic function is adopted to fit the sampled curve with 3 coefficients a_0,a_1 and a_2 as shown in (A.1). With least square optimization $\mathbf{d} = [a_0, a_1, a_2]^T$ is estimated and the value is given in (A.2)

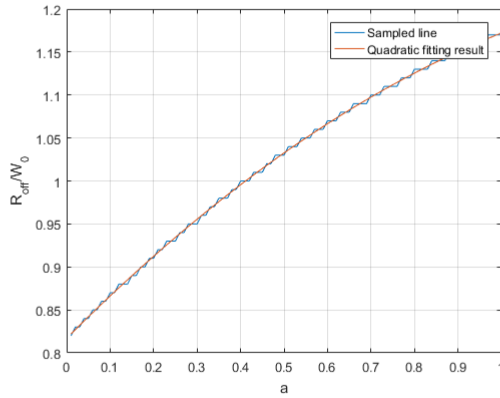

Fig. A.2. Functional relationship between r_h and R'_{off}

$$R'_{off} = a_2 r_h^2 + a_1 r_h + a_0 \quad \text{(A.1)}$$

$$[a_0, a_1.a_2] = [0.81701, 0.50713, -0.15195] \quad \text{(A.2)}$$

APPENDIX B
DERIVATION OF $f(S_{rltexp})$

As Figure B.3 shows, even with same average value in the homogeneous area, the smoothness relies heavily on the density of the Gaussian profiles. i.e. the value of hatching space ratio a can affect the homogeneity of the exposure in middle area.

To make exposure smoothness well defined, the definition of relative variance S_{rltexp} is given in (B.3). E_{ave} is the average value of the exposure value in the middle area, which is shown as the plateau in Figure B.3. And in numerical simulation, to ensure that the points sampled for the calculation of E_{ave} and V_{exp}, the sampled points are designated to be those within interval $[-2, 2]$. S_{exp} is the standard deviation of the exposure values in the homogeneous area. By dividing S_{exp} with E_{ave}, the effect of homogeneous exposure on the exposure standard deviation are eliminated. And larger the value of S_{rltexp} is, more rough the plateau exposure profile is. i.e. the relative smoothness is given by the standard deviation of exposure

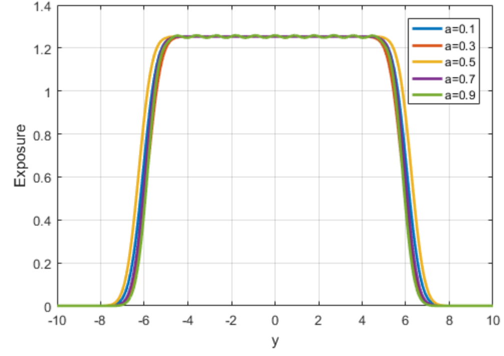

Fig. B.3. The exposure profile with different hatching space ratio a and same average value in homogeneous area

values in homogeneous area.

$$S_{rltexp} = \frac{S_{exp}}{E_{ave}} \quad \text{(B.3)}$$

Usually, the aimed mechanical properties of the product has some requirements on the homogeneity of the exposure and with an equation between S_{rltexp} and a, the value of a can be determined. The relationship between S_{rltexp} and a is given in Figure B.4 by calculating the values of S_{exp} with different a value.

The curve in Figure B.4 is approached with formula given

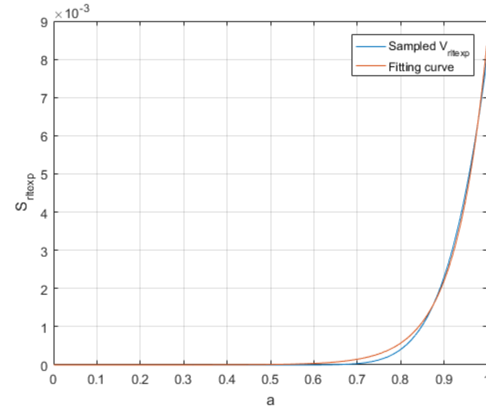

Fig. B.4. Functional relationship between hatching space ratio a and relative standard deviation S_{relexp}

in (B.4) and the value of undetermined constants are given in (B.5)

$$S_{rltexp} = c_1 + c_2 e^{c_3 a + c_4} \quad \text{(B.4)}$$

$$\begin{bmatrix} c_1 \\ c_2 \\ c_3 \\ c_4 \end{bmatrix} = \begin{bmatrix} 0.000000000001609 \\ 0.000000005624445 \\ 13.533366236195040 \\ 0.699163599010420 \end{bmatrix} \quad \text{(B.5)}$$

APPENDIX C
DERIVATION OF SCAN VELOCITY V_s

Given Gaussian laser beam with Gaussian radius W_{e3D} and power P_L, the profile of the exposure with ACES scanning can

give an area with approximately homogeneous distribution of the exposure as shown in Figure C.5. The exposure given by

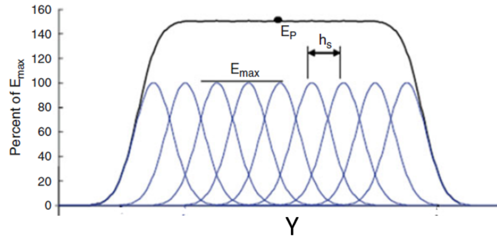

Fig. C.5. The exposure profile given by ACES scanning with Gaussian laser beam. Laser power is P_L. Gaussian radius is W_{e3D}. The exposure of single line scanning is E_{max} and the exposure in the middle area is E_p. h_s is the distance between the centers of the neighboring scanning lines. Figure is Adopted from [3]

a single line scanning can be calculated by (C.6), [3]. The coordinate origin is located at the center of scanning line for simplicity.

$$E_s(y) = \sqrt{\frac{2}{\pi}} \frac{P_L}{W_{e3D} V_s} e^{-2y^2/W_{e3D}^2} \tag{C.6}$$

And the exposure value of E_p in ACES can be calculated by (C.7).

$$E_p = \sqrt{\frac{2}{\pi}} \frac{P_L}{W_{e3D} V_s} \sum_{l=-\infty}^{l=\infty} e^{-2(lr_h)^2} \tag{C.7}$$

The value of E_{p1} approximates the average exposure exposure in an infinite plate printed with ACSE scanning pattern. And the value of average exposure exposure can be calculated by equation (C.8).

$$\begin{aligned} E_p &= \sqrt{\frac{2}{\pi}} \frac{P_L}{W_{e3D} h_s V_s} \int_{y=-\infty}^{y=+\infty} e^{-2y^2/W_{e3D}^2} dy \\ &= \frac{P_L}{V_s h_s} \end{aligned} \tag{C.8}$$

According to the solution in (C.8), for given target exposure E_tar, the velocity for scanning should be the value calculated by (C.9)

$$V_s = \frac{P_L}{E_{tar} h_s} \tag{C.9}$$

Acknowledgment

Sincere appreciation to Schafer for his code of [23], [24] Mie theory calculator and Yarpiz for his [29] code of ACO. Thanks for your contribution in my project. And great thanks to my tutor Thomas Hafkamp and my supervisor Bram de Jager, Thank you for your priceless guidance and your precious time.

References

[1] P. Jacobs, *Stereolithography and other RP & M technologies*, 1st ed. Dearborn, Dearborn, MI: Society of Manufacturing Engineers in cooperation with the Rapid Prototyping Association of SME, 1996.

[2] P. F. Jacobs and D. T. Reid, *Rapid prototyping & manufacturing: fundamentals of stereolithography*, 1st ed. Society of Manufacturing Engineers, 1992.

[3] I. Gibson, D. W. Rosen, and B. Stucker, *Additive Manufacturing Technologies: 3D Printing, Rapid Prototyping,and Direct Digital Manufacturing*, 2nd ed. New York: Springer, 2015. Chap. 1.

[4] J. W. Halloran, *Ceramic Stereolithography: Additive Manufacturing for Ceramics by Photopolymerization*. Annual Review of Materials Research, vol. 46, no. 1, 2016, pp. 19-40

[5] J. W, Halloran, *Freeform fabrication of ceramics*. British Ceramic Transactions, vol. 98, no. 6, pp. 299-303

[6] A. Gebhardt, *Generative Fertigungsverfahren: Additive Manufacturing und 3D Drucken für Prototyping-Tooling-Produktion*, Aufl. München: Hanser, 2013

[7] G. Mitteramskogler, R. Gmeiner, R. Felzmann, S. Gruber, C. Hofstetter, J. Stampfl, J. Ebert, W. Wachter, and J. Laubersheimer, *Light curing strategies for lithography-based additive manufacturing ofcustomized ceramics*. Additive Manufacturing, vol. 1-4, 2014, pp. 110-118

[8] M. Dehurtevent, L. Robberecht, J.-C. Hornez, A. Thuault, E. Deveaux, and P. Béhin, Pascal, *Stereolithography: A new method for processing dental ceramics by additive computer-aided manufacturing*. Dental Materials, vol. 33, no. 5, 2017, pp. 477-485

[9] T. Hafkamp, G. V. Baars, B. D. Jager, and P. Etman, *A feasibility study on process monitoring and control in vat photopolymerization of ceramics*. Mechatronics, 2018

[10] D. W. Hahn, *Light scattering theory*. Department of Mechanical and Aerospace Engineering, Florida, 2006

[11] A. S. Martinez and T. J. Arruda, *A set of basis functions to improve numerical calculation of Mie scattering in the Chandrasekhar-Sekera representation*. arXiv preprint physics/0605058, 2006

[12] A. Gu and A. Zakhor, *Optical proximity correction with linear regression*. IEEE Transactions on Semiconductor Manufacturing, vol. 21, no. 2, 2008 ,pp. 263-271

[13] H. C. Hulst and H. C. van de Hulst, Hendrik C, *Light scattering by small particles*. Courier Corporation, 1981

[14] C. Sun and X. Zang, *Experimental and numerical investigations on microstereolithography of ceramics*. Journal of Applied Physics, vol. 92, no. 8, 2002 ,pp. 4796-4802

[15] S. Gentry, *Factors affecting the resolution of photopolymerized ceramics*. Ann Arbor (MI): University of Michigan, 2012

[16] R. E. Bellman, *Dynamic programming treatment of the travelling salesman problem*. Journal of the ACM (JACM), vol. 9, no. 1, 1962 ,pp. 61-63

[17] M. Held and R. M. Karp, *The traveling-salesman problem and minimum spanning trees*. Operations Research, vol. 18, no. 6, 1970 ,pp. 1138-1162

[18] M. Held, and R. M. Karp, *The traveling-salesman problem and minimum spanning trees: Part II*. Mathematical programming, vol. 1, no. 1, 1971 ,pp. 6-25

[19] M. Dorigo and L. M. Gambardella, *Ant colonies for the travelling salesman problem*. biosystems, vol. 43, no. 2, 1997 ,pp. 73-81

[20] Z. Ye, X. Jiang and Z. Wang, *Measurements of Particle Size Distribution Based on Mie Scattering Theory and Markov Chain Inversion Algorithm.*. JSW, vol. 7, no. 10, 2012 ,pp. 2309-2316

[21] Q. Fu and W. Sun, *Mie theory for light scattering by a spherical particle in an absorbing medium*. Applied Optics, vol. 40, no. 9, 2001 ,pp. 1354-1361

[22] O. Mengual, G. Meunier, I. Cayré, K. Puech and P. Snabre, *TURBISCAN MA 2000: multiple light scattering measurement for concentrated emulsion and suspension instability analysis*. Talanta, vol. 50, no. 2, 1999 ,pp. 445-456

[23] J. P. Schäfer, *Implementierung und Anwendung analytischer und numerischer Verfahren zur Lösung der Maxwellgleichungen für die Untersuchung der Lichtausbreitung in biologischem Gewebe*. Universität Ulm. Fakultät für Naturwissenschaften, PhD thesis, 2011

[24] J. Schfer, S. C. Lee, and A. Kienle, *Calculation of the near fields for the scattering of electromagnetic waves by multiple infinite cylinders at perpendicular incidence*. Journal of Quantitative Spectroscopy and Radiative Transfer, vol. 113, no. 16, 2012 ,pp. 2113–2123

[25] C. Mätzler, *MATLAB functions for Mie scattering and absorption, version 2*. IAP Res. Rep, vol. 8, no. 1, 2002

[26] Irina.eas.gatech.edu (2018). [online] Available at:http://irina.eas.gatech.edu/EAS8803_Fall2009/Lec15.pdf [Accessed: 21- Oct- 2018].

[27] Astro.umd.edu (2018). [online] Available at:https://www.astro.umd.edu/ miller/teaching/astr601f14/lecture03.pdf. [Accessed: 21- Oct- 2018].

[28] ”MatScat - File Exchange - MATLAB Central”, Mathworks.com, 2018. [Online]. Available: https://www.mathworks.com/matlabcentral/fileexchange/36831-matscat. [Accessed: 23- Oct- 2018]. matfileexc

[29] Ant Colony Optimization (ACO) - File Exchange - MATLAB Central, Mathworks.com, 2018. [Online]. Available:

https://www.mathworks.com/matlabcentral/fileexchange/52859-ant-colony-optimization-aco. [Accessed: 06- Nov- 2018].

Technische Universiteit **Eindhoven** University of Technology

Declaration concerning the TU/e Code of Scientific Conduct for the Master's thesis

I have read the TU/e Code of Scientific Conduct[i].

I hereby declare that my Master's thesis has been carried out in accordance with the rules of the TU/e Code of Scientific Conduct

Date

8th November, 2018
....

Name

Zhihao Wu
....

ID-number

1041226
....

Signature

Zhihao Wu
....

Submit the signed declaration to the student administration of your department.

[i] See: http://www.tue.nl/en/university/about-the-university/integrity/scientific-integrity/
The Netherlands Code of Conduct for Academic Practice of the VSNU can be found here also.
More information about scientific integrity is published on the websites of TU/e and VSNU